Rare Metal Materials and Engineering
Volume 54, Issue 7, July 2025
Available online at www.rmme.ac.cn

Science Press

Cite this article as: Yang Run, Wang Hui, Liu Rui, et al. Microstructure and Properties of ZrC Nanoparticles-Strengthened WNiFe Alloys[J]. Rare Metal Materials and Engineering, 2025, 54(07): 1661-1670. DOI: https://doi.org/10.12442/j.issn.1002-185X.20240635.

ARTICLE

Microstructure and Properties of ZrC Nanoparticles-Strengthened WNiFe Alloys

Yang Run[1,2], **Wang Hui**[2], **Liu Rui**[1,2], **Wu Xuebang**[2], **Wang Xianping**[2], **Fang Qianfeng**[1,2], **Liu Changsong**[2]

[1] University of Science and Technology of China, Hefei 230026, China; [2] Institute of Solid State Physics, Hefei Institutes of Physical Science, Chinese Academy of Sciences, Hefei 230031, China

Abstract: 93W-4.9Ni-2.1Fe alloys strengthened by nanoscale ZrC particles were prepared by spark-plasma-sintering (SPS) and hot rotary swaging, separately. Results show that the addition of a small number of ZrC nanoparticles can refine grains and increase the hardness of the WNiFe alloys, but hinder the formation of the γ-(Ni, Fe) phase during SPS. SPSed WNiFe and WNiFe-ZrC alloys are brittle at room temperature, while the swaged WNiFe and WNiFe-0.5ZrC (wt%) alloys are ductile. At 400 °C, the swaged WNiFe-0.5ZrC alloy exhibits both higher tensile strength and better ductility than the swaged WNiFe. The nanoscale particles distributed in the W grains and γ-(Ni, Fe) phase provide a good pinning effect, which enhances the strength. The thermal conductivity of swaged WNiFe-0.5ZrC is only 71 $W\cdot m^{-1}\cdot K^{-1}$ at room temperature, but it increases to about 100 $W\cdot m^{-1}\cdot K^{-1}$ at 800 °C, which is close to that of pure W (121 $W\cdot m^{-1}\cdot K^{-1}$). These results show the potential of WNiFe alloys as plasma-facing materials in fusion reactor.

Key words: tungsten alloy; ZrC; dispersion strengthening; microstructure; thermal conductivity

1 Introduction

Tungsten (W) with high melting temperature, high thermal conductivity, low tritium retention and low sputter yield has been considered as one of the most promising plasma-facing materials (PFMs) in future fusion reactors and suitable target materials for spallation neutron source[1–3]. However, pure W exhibits shortcomings such as room temperature (RT) brittleness, recrystallization embrittlement and irradiation-induced embrittlement, which greatly restrict its applications[4–6].

In recent years, W heavy alloys (WHAs) have been investigated as a substitute for pure W PFMs due to their room temperature ductility and lower cost[7–9]. WHAs is a typical bi-phase metallic composite, consisting of body-centered cubic (bcc) W particles embedded in ductile γ-(Ni, Fe) matrix phase with face-centered cubic (fcc) structure. Compared to the pure W, the existence of ductile γ-(Ni, Fe) phase is favorable for WHAs to improve the room temperature ductility[10]. Neu et al[7–8] reported that the magnetic properties and thermal conductivity of WHAs satisfy the necessary criteria for utilization in fusion reactor applications, and these properties do not contribute to an elevation in the Fe/Ni content within the plasma during typical operational circumstances. However, extremely high-temperature environment still poses a significant challenge to WHAs. The interfacial strength of W-matrix will be dramatically decreased at elevated temperatures due to the relatively low melting temperature of γ-(Ni, Fe) (approximately 1450 °C) [11–13]. Therefore, the strength of WHAs at elevated temperatures needs further improvement.

The dispersion of high-melting-temperature nanoscale oxides (such as Y_2O_3[14–15] and La_2O_3[16]) or carbides (such as ZrC[17] and TiC[18]) into W can refine the grains and improve the strength and recrystallization temperature of W alloys. Among these strengthening phases, ZrC particles have high melting temperature (3540 °C), high hardness and low

---

Received date: September 30, 2024
Foundation item: National Key Research and Development Program of China (2022YFE03140002, 2019YFE03110200); National Natural Science Foundation of China (52273320, 52173303, 52325103, 52171084); Strategic Priority Research Program of the Chinese Academy of Sciences (XDB0470000); Anhui Provincial Natural Science Foundation (2308085J07); HFIPS Director's Fund (YZJJ202102, YZJJQY202306, YZJJKX202202)
Corresponding author: Liu Rui, Ph. D., Professor, Institute of Solid State Physics, Hefei Institutes of Physical Science, Chinese Academy of Sciences, HeFei 230031, P. R. China, Tel: 0086-551-65591727, E-mail: liurui@issp.ac.cn

activation, and they can react with impurity oxygen to form stable particles, alleviating the detrimental effect of O on grain boundary cohesion. As a result, W and Mo alloys strengthened by ZrC exhibit high strength, low ductile-to-brittle transition temperature (DBTT) and high recrystallization temperature[19–20]. Moreover, W alloys strengthened by ZrC nanoparticles also exhibit enhanced resistance to neutron irradiation[21–22].

WHAs strengthened by ZrC particles also attract research interests. For example, 75WNiFe-1ZrC prepared by liquid phase sintering (LPS) exhibited a high tensile strength of 847 MPa and a total elongation of 18.8% at RT[23], but the high content of γ-(Ni, Fe) would significantly reduce the thermal conductivity, which cannot meet the requirements of thermal shock resistance for PFMs. Sun et al[24] prepared ZrC nanoparticles-strengthened 90WNiFe alloy by pressureless sintering, and it exhibits enhanced hardness (351 HV) and compressive strength (2179 MPa) at RT compared to 90WNiFe (302 HV, 1570 MPa). Nevertheless, the tensile properties at elevated temperature and thermal conductivity of ZrC-strengthened WNiFe alloys have rarely been investigated, which are necessary for WHAs to be used as PFMs in nuclear fusion devices.

In this work, nanoscale ZrC particles were introduced into WNiFe (93W-4.9Ni-2.1Fe) alloys to improve the mechanical properties and thermal stability. Fine-grained WNiFe alloys with different ZrC contents were prepared by spark plasma sintering (SPS) to optimize the alloy composition, and WNiFe-ZrC alloy rods with enhanced mechanical properties were prepared through LPS and hot rotary swaging. The microstructure, mechanical properties and thermal conductivity of WNiFe-ZrC alloys at different temperatures were investigated to evaluate their feasibility as PFMs.

2 Experiment

Commercial W powders (about 600 nm, purity>99.98%), Ni powders (about 100 nm, purity>99.7%), Fe powders (1–3 μm, purity>99.5%) and nanoscale ZrC powders (about 50 nm, purity>99%) were used as starting materials. The ratio of W:Ni:Fe in WNiFe alloys is 93.0:4.9:2.1, and the content of ZrC is 0.25wt%, 0.5wt% and 0.75wt%. The powders were mixed in a planetary ball mill in argon atmosphere at 240 r/min for 4 h, and the ball to powder ratio was 10:1. After ball milling, the powders were loaded into a graphite mold with a diameter of 30 mm. SPS (SE-607, FCT Group, Germany) was used for rapid densification of powders. Firstly, the samples were heated to 750 °C under 50 MPa and held for 10 min in vacuum atmosphere. Subsequently, the samples were further heated up to 1100–1300 °C in a flowing argon atmosphere with a heating rate of 100 °C/min, held for 8 min, and then cooled to RT at a cooling rate of 100 °C/min.

WNiFe and WNiFe-0.5%ZrC alloy rods were also prepared by hot rotary swaging. Firstly, the ball-milled powders were compacted into cylindrical rods by cold isostatic pressing and sintered at 1450 °C in a flowing hydrogen atmosphere. Then, the sintered rods were subject to hot swaging at 1100 °C, and the area reduction was about 16% after two passes of swaging. The diameter of swaged (SW) WNiFe-ZrC alloys was about 10.0 mm.

Electron backscatter diffractometer (EBSD, Oxford Instruments, C-Nano, UK) was used to characterize the grain size distribution and orientation of WNiFe and WNiFe-ZrC. For the preparation of EBSD samples, the samples were firstly polished using diamond paper and finally vibrationally polished by oxide suspension of 2.5 μm to remove the surface stress layer. Misorientation angle θ>10° was used to distinguish the grain boundaries. X-ray diffraction (XRD) analysis was conducted with an X'pert Pro MPD diffractometer with Cu Kα radiation. Transmission electron microscope (TEM, FEI Talos F200X) was employed to analyze the size and distribution of nanoscale particles, and high-resolution transmission electron microscope (HRTEM) was employed to characterize the particles and matrix. Field emission scanning electron microscope (SEM, SU8020 Hitachi, Japan) was used to observe the fracture morphology of WNiFe-ZrC alloys after tensile testing, and the energy-dispersive X-ray spectroscope (EDS) installed on SEM was used for elemental analysis.

The samples were cut by electric discharge machining and then mechanically polished for hardness measurements and tensile tests. The hardness measurements were conducted at RT by a Vickers microhardness tester with a load of 500 g and a dwell time of 15 s. Tensile tests were performed on an Instron-5967 machine at temperatures ranging from RT to 400 °C with a strain rate of 2×10^{-4} s^{-1}. Tensile test samples were prepared with a cross section of 1.5 mm×0.5 mm and a gauge length of 5 mm. Thermal conductivity test was performed by a laser flash analyzer instrument (LFA 467, Netzsch).

3 Results and Discussion

3.1 Microstructure and mechanical properties of SPS WNiFe-ZrC alloys

Fig. 1 shows EBSD images of WNiFe alloys with different ZrC contents prepared by SPS. Table 1 lists the relative density, average grain size and microhardness values of SPS WNiFe and SPS WNiFe-xZrC (x=0.25, 0.5, 0.75, wt%) alloys. The relative density of SPS WNiFe and SPS WNiFe-xZrC samples is higher than 96%, and the relative density increases gradually with the increase in ZrC content. The SPS WNiFe exhibits fine equiaxed grains with an average grain size of 1.64 μm, which could be attributed to the relatively low sintering temperature and short sintering time. The average grain size of SPS WNiFe-0.25ZrC and SPS WNiFe-0.5ZrC is 1.51 and 1.42 μm, respectively. These results indicate that the addition of a small number of ZrC nanoparticles can effectively refine grains of WNiFe alloys. However, when the ZrC content increases to 0.75wt%, the grain is not further refined. The average grain size of SPS WNiFe-0.75ZrC (1.46 μm) is slightly larger than that of WNiFe-0.5ZrC (1.42 μm), and large grains and small grains began to differentiate significantly. This may be due to the non-uniform dispersion

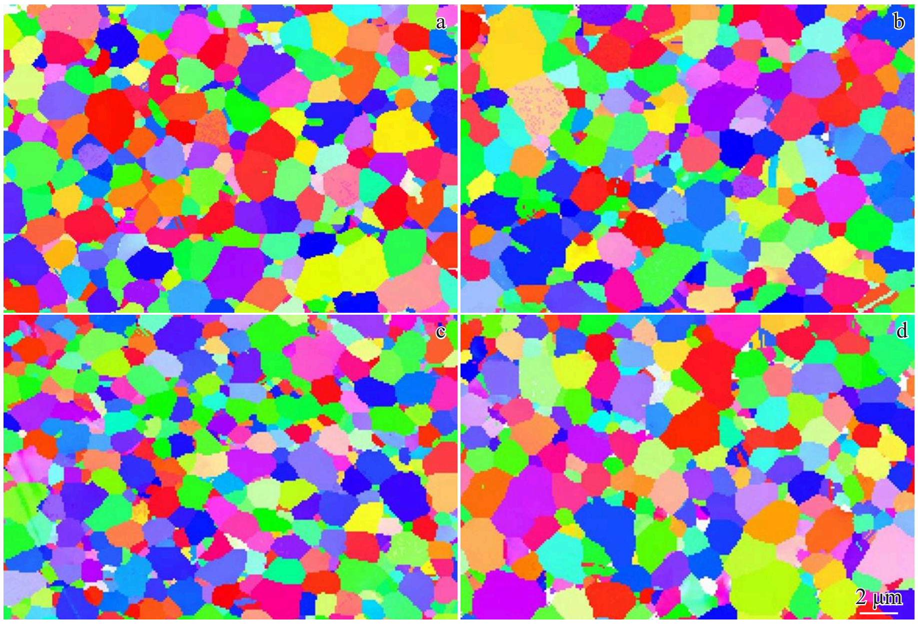

Fig.1 EBSD images of WNiFe (a), WNiFe-0.25ZrC (b), WNiFe-0.5ZrC (c), and WNiFe-0.75ZrC (d) samples prepared by SPS

Table 1 Density, relative density, average grain size and microhardness of WNiFe and WNiFe-ZrC alloys prepared by SPS

Materials	Density/g·cm^{-3}	Relative density/%	Average grain size/μm	Microhardness/HV
SPS WNiFe	17.10	96.18	1.64±0.52	422.6±4.7
SPS WNiFe-0.25ZrC	17.04	96.22	1.51±0.50	435.5±5.6
SPS WNiFe-0.5ZrC	17.05	96.69	1.42±0.47	456.7±8.7
SPS WNiFe-0.75ZrC	16.99	96.72	1.46±0.57	449.4±7.0
SW WNiFe	17.60	98.99	37.13±13.0	361.5±10.8
SW WNiFe-0.5ZrC	17.22	98.03	23.33±9.5	393.8±11.8

of ZrC nanoparticles within the WNiFe alloy.

The content and distribution of γ-(Ni, Fe) phase are the main indicators determining the mechanical properties of WNiFe alloys. Fig.2 shows XRD patterns of SPS WNiFe and SPS WNiFe-xZrC alloys. The characteristic peak at 43.49° corresponding to (111) plane of γ-(Ni, Fe) phase can be clearly detected in SPS WNiFe sample, indicating that elements Ni and Fe form γ-(Ni, Fe) phase during sintering process. Nevertheless, the characteristic peak of the γ-(Ni, Fe) phase is not found in the samples containing ZrC nanoparticles. The reason may be that ZrC nanoparticles hinder the formation of γ-(Ni, Fe) phase during solid-phase sintering process.

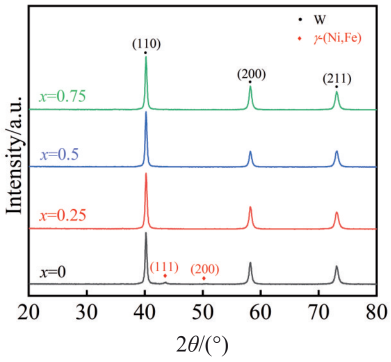

Fig.2 XRD patterns of WNiFe-xZrC alloys prepared by SPS (x=0, 0.25, 0.5, 0.75, wt%)

The microhardness of SPS WNiFe and SPS WNiFe-0.25ZrC is 422.6 and 435.5 HV, respectively (Table 1). The SPS WNiFe-0.5ZrC exhibits the highest microhardness of 456.7 HV. When the ZrC content is further increased to 0.75wt%, the microhardness of SPS WNiFe-0.75ZrC alloy is 449.4 HV, which is comparable to that of SPS WNiFe-0.5ZrC. The samples with smaller grain size exhibit higher microhardness, which is reasonable according to the Hall-Petch relationship.

Tensile testing results show that the SPS WNiFe alloy is brittle at RT with a fracture strength of 790 MPa. Contrary to expectations, the SPS WNiFe-0.5ZrC and SPS WNiFe-0.75ZrC samples fracture at relatively low stress of 437 and 337 MPa, respectively. Fig.3 shows the RT fracture morphologies of SPS WNiFe and SPS WNiFe-xZrC samples. The fracture surface of SPS WNiFe (Fig.3a) shows that the grains are uniformly surrounded by binding phase and the fracture mode is composed of intergranular fracture and transgranular fracture. When the ZrC content increases to 0.25wt% and 0.75wt%, the proportion of binding phase decreases gradually, and the fracture mode is dominated by intergranular fracture,

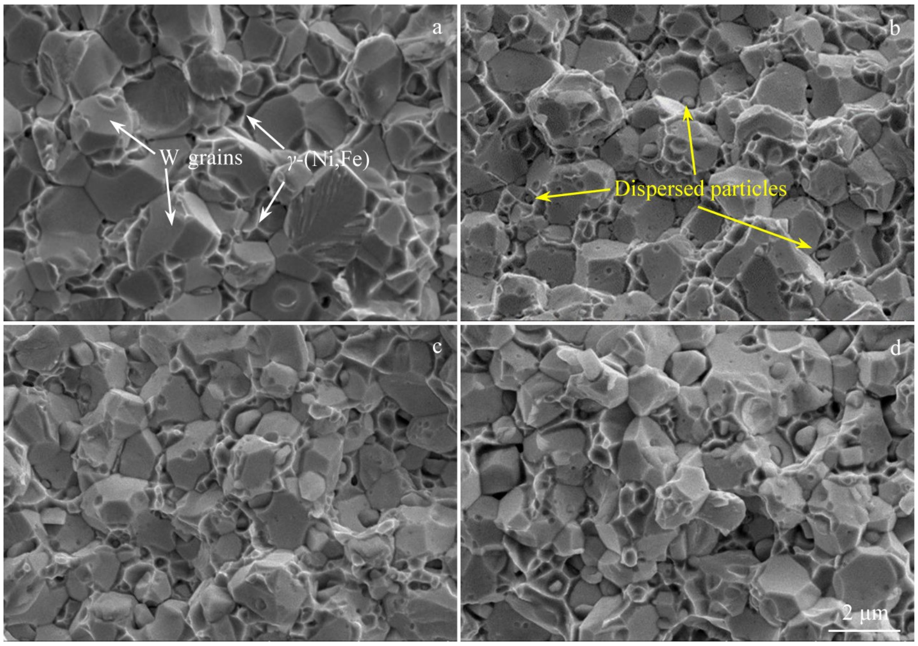

Fig.3 SEM micrographs of tensile fracture surfaces of WNiFe (a), WNiFe-0.25ZrC (b), WNiFe-0.5ZrC (c), and WNiFe-0.75ZrC (d) prepared by SPS

as shown in Fig.3b–3d. EDS element mapping results in Fig.4 show the distribution of γ-(Ni, Fe) phase in SPS WNiFe and SPS WNiFe-ZrC alloys. C_{WW} is a connectivity indicator in WHAs that characterizes the adjacency between W grains. Due to the high consistency between the distribution of elements Ni and Fe, the distribution of element Ni is chosen to show the distribution of γ-(Ni, Fe) phases. It can be seen that the γ-(Ni, Fe) phase in the SPS WNiFe is mainly dispersed around the W grains in the form of stripes/spheres, while the addition of ZrC nanoparticles reduces the stripes in the γ-(Ni, Fe) phase, which reduces the contact area of the matrix phase with the W grains and thus leads to the degradation of the mechanical properties. These results indicate that the addition of ZrC nanoparticles can refine grains and improve the microhardness of WNiFe alloys, but suppress the formation of γ-(Ni, Fe) phase during SPS, especially at relatively low temperatures.

Fig. 5 shows TEM and HRTEM images of SPS WNiFe-0.5ZrC. It can be seen that nanoscale particles with an average particle size of about 74 nm are distributed inside grains and at grain boundaries, as indicated by bright-field and dark-field TEM images in Fig. 5a and 5b, respectively. In Fig. 5c, HRTEM and fast Fourier transform (FFT) results show that the nanoscale particles are predominantly monoclinic ZrO_2 (m-ZrO_2). These results indicate that the initial ZrC nanoparticles convert into m-ZrO_2 during the SPS process, which could be attributed to the reaction of ZrC with impurity oxygen. ZrC, as an oxygen getter, can react with impurity oxygen to form stable ZrO_2 particles and to alleviate the detrimental effect of oxygen on grain boundaries[20]. These nanoscale particles can improve the strength and thermal stability by pinning dislocations and grain boundaries. HRTEM images and corresponding FFT results in Fig.5d–5f demonstrate that the phases distributed on the interface are W grains and γ-(Ni, Fe) phase.

3.2 Microstructure of SW WNiFe-ZrC alloy

The results of WNiFe-ZrC alloys prepared by SPS indicate that the addition of ZrC nanoparticles can effectively refine the grains, but the WNiFe-ZrC samples are brittle at RT with relatively low tensile strength. In order to improve the

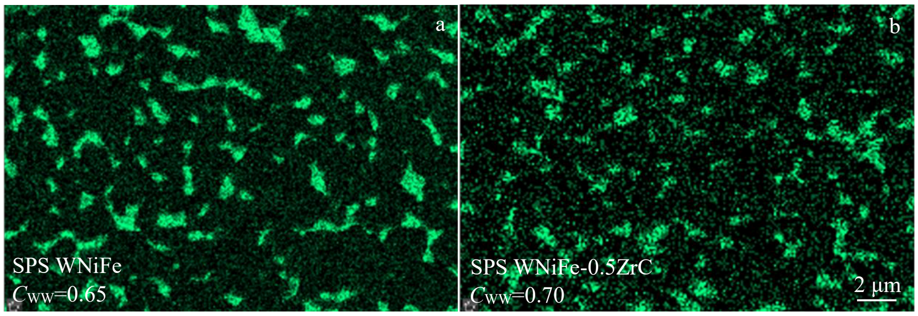

Fig.4 EDS element mapping results of γ-(Ni,Fe) phase in WNiFe (a) and WNiFe-0.5ZrC (b) prepared by SPS

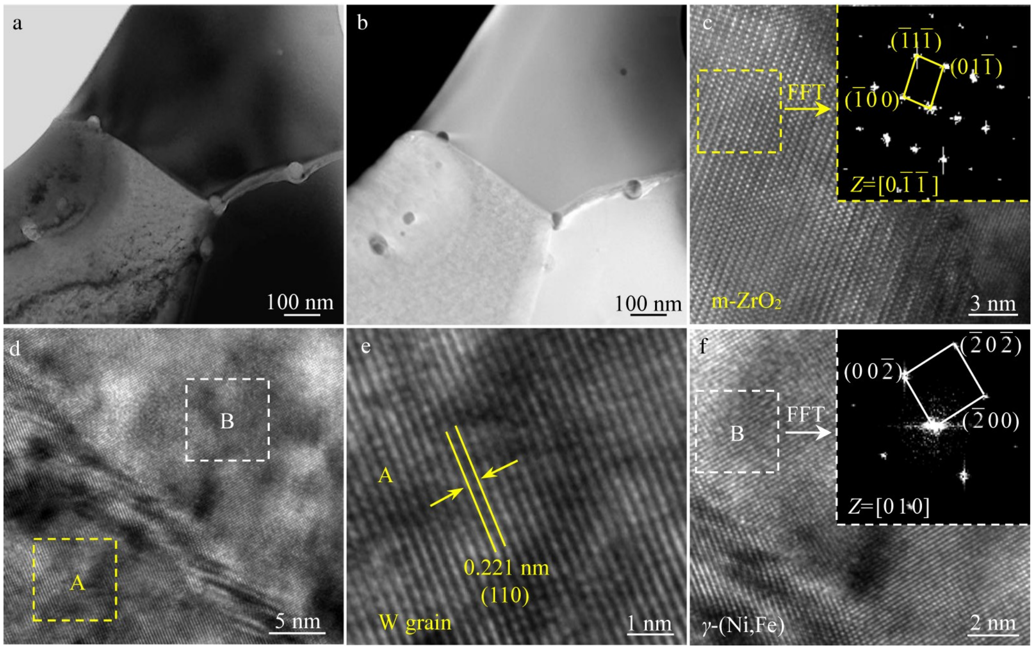

Fig.5 Bright-field (a) and dark-field (b) TEM images of SPS WNiFe-0.5ZrC; HRTEM images and corresponding FFT results of m-ZrO_2 (c), W/γ-(Ni, Fe) interface (d), W grain (e), and γ-(Ni, Fe) (f)

mechanical properties of WNiFe-ZrC alloy, LPS and hot rotary swaging were employed for the fabrication of WNiFe-ZrC alloy. Fig.6 shows EBSD results of SW WNiFe and SW WNiFe-0.5ZrC alloys parallel to longitudinal direction. Due to the small deformation of hot rotary swaging process (area reduction of about 16%), the anisotropy of the grains is not significant. After LPS and rotary swaging, the relative density of WNiFe and WNiFe-0.5ZrC increases to 98.99% and 98.03% (Table 1), respectively, and their grains grow significantly. The SW WNiFe alloy exhibits an average grain size of 37.1 μm, while the SW WNiFe-0.5ZrC alloy has an average grain size of 23.3 μm. The average grain size of SW WNiFe and SW WNiFe-ZrC samples is much larger than that of SPS ones, which can be attributed to the higher sintering temperature. The SW WNiFe-0.5ZrC has higher microhardness (393.8 HV) than SW WNiFe (361.6 HV). However, the microhardness values of both SW alloys are lower than those of SPS ones, which is attributed to the larger grain size.

Fig. 7a – 7b shows SEM images of SW WNiFe and SW WNiFe-0.5ZrC alloys. It can be seen that near spherical W

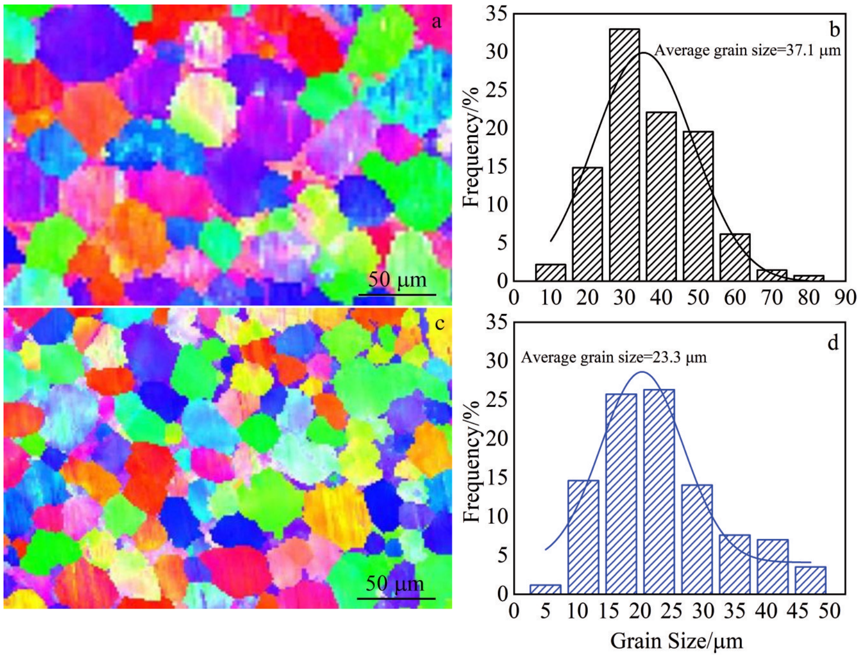

Fig.6 EBSD results (a, c) and grain size distributions (b, d) of SW WNiFe (a–b) and SW WNiFe-0.5ZrC (c–d)

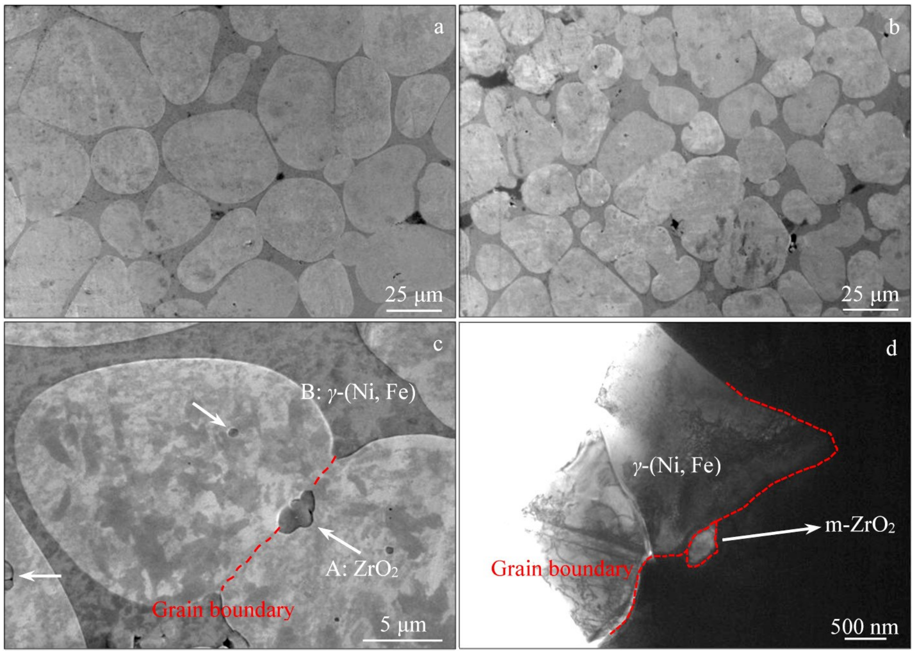

Fig.7 SEM images of SW WNiFe (a) and SW WNiFe-0.5ZrC (b–c); TEM image of m-ZrO_2 particle located at interface between W grain and γ-(Ni, Fe) phase (d)

grains are embedded in γ-(Ni, Fe) matrix phases, and the addition of ZrC nanoparticles effectively refines the grains of WNiFe alloy. As compared with SPS samples, SW WNiFe and SW WNiFe-0.5ZrC exhibit near spherical W particles with continuous distribution of binding phases, which can be explained by the Ostwald ripening mechanism, as the flowing matrix phase is more conducive to mass transfer processes. For the SW WNiFe-0.5ZrC, the dispersed particles are distributed within and between the grains, as indicated by white arrows in Fig. 7c. For the particle located at grain boundary (indicated by A), Zr and O signals are detected according to EDS results, indicating that the particle is ZrO_2. Fig. 7d shows TEM image of m-ZrO_2 particle located at the interface between W phase and γ-(Ni, Fe) phase. The presence of ZrO_2 particles indicates that ZrC nanoparticles react with impurity oxygen, which is consistent with the result of Fig.7c. These dispersed particles at the interface between W grains (W-W) and between W grain and γ-(Ni, Fe) matrix phase (W-M) can hinder the grain growth during the sintering process, leading to refined grains. The grain coarsening during LPS can be explained by the kinetic equation[25]:

$$G_0^n + Kt = G^n \tag{1}$$

where G_0 is the initial grain size, K is the rate of grain coarsening, t is the isothermal time, G is the grain size after sintering, and n is usually 3. The average grain size of SW WNiFe and SW WNiFe-0.5ZrC is 37.1 and 23.3 μm, respectively. By calculating the ratio of K, it can be learned that the grain coarsening rate of SW WNiFe is about four times of that of SW WNiFe-0.5ZrC at 1450 °C. This result indicates that the addition of ZrC nanoparticles can effectively inhibit the grain growth.

Fig. 8 shows EDS element mapping of γ-(Ni, Fe) phase in SW WNiFe and SW WNiFe-0.5ZrC alloys. During LPS process, the γ-(Ni, Fe) phase uniformly encapsulates around the W grains, which significantly improves the ratio of the W-M interface in SW WNiFe alloy, as shown in Fig.8a. As for SW WNiFe-0.5ZrC alloy, the introduction of ZrC nanoparticles leads to refined W grains, and the increased grain

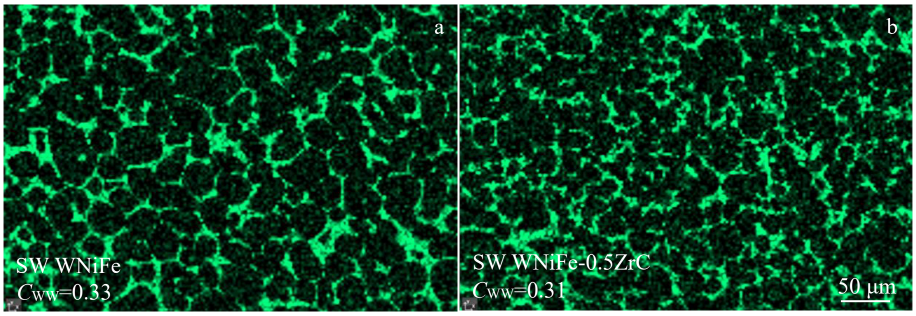

Fig.8 EDS element mapping results of γ-(Ni, Fe) phase distribution in SW WNiFe (a) and SW WNiFe-0.5ZrC (b)

boundaries increase the ratio of W-M interface. C_{WW} can be obtained using the line intercept method, as follows:

$$C_{\mathrm{WW}} = \frac{2N_{\mathrm{WW}}}{N_{\mathrm{WM}} + 2N_{\mathrm{WW}}} \tag{2}$$

where N_{WW} is the number of interfaces between W and W grains, and N_{WM} is the number of W-M interfaces. The interfacial relationships in alloys were quantified by means of a metric such as the adjacency C_{WW}. In the case of SPS samples, the addition of ZrC nanoparticles suppressed the formation of γ-(Ni, Fe) phase to a certain extent, so the C_{WW} increased from 0.65 to 0.70 after the addition of 0.5wt% ZrC (Fig. 4). The C_{WW} of SW WNiFe and SW WNiFe-0.5ZrC samples is 0.33 and 0.31, respectively. The low C_{WW} of SW WNiFe-0.5ZrC could be attributed to LPS process that promotes the formation of the γ-(Ni, Fe) phase and the fact that the addition of ZrC nanoparticles effectively refines the grains and improves the number of interfaces.

3.3 Mechanical properties of SW WNiFe and SW WNiFe-0.5ZrC alloys

Fig. 9 shows the engineering stress-engineering strain curves of SW WNiFe and SW WNiFe-0.5ZrC alloys during tensile test at RT, 200 °C and 400 °C. At RT, the ultimate tensile strength (UTS) and total elongation (TE) of SW WNiFe are 1059 MPa and 13.0%, respectively. SW WNiFe-0.5ZrC exhibits a higher UTS of 1098 MPa and a TE of 9.3%. At 200 °C, the UTS of SW WNiFe-0.5ZrC is 959 MPa, which is also higher than that of SW WNiFe (915 MPa). When the temperature is further increased to 400 °C, the strengthening effect of ZrC is more obvious. The UTS of SW WNiFe-0.5ZrC and SW WNiFe at 400 °C is 859 and 774 MPa, respectively. The SW WNiFe-0.5ZrC exhibits both higher strength and higher elongation than SW WNiFe at 400 °C.

With regard to the factors affecting strength in WHAs, it is suggested that the yielding in two-phase WHAs begins with the deformation of the γ-(Ni, Fe) matrix phase[26]. The yield strength can be expressed as follows[27]:

$$\sigma_{\mathrm{y}} = \sigma_0 + K\left[\frac{C_{\mathrm{WW}}\left(1 - V_{\mathrm{m}}\right)}{dV_{\mathrm{m}}}\right]^{\frac{1}{2}} \tag{3}$$

where σ_{y} is the yield strength of WHAs, σ_0 and K are non-negative constants, C_{WW} is the adjacency index between W and W, V_{m} is the volume fraction of the matrix phase, and d is the size of the W grain. For ease of description, the value to the right of K is abbreviated as P. Armstrong et al[28] indicates the meaning of the K value: taking σ_{y} as the Y-axis and P as the X-axis, K is the Hall-Petch slope, and the magnitude of the slope value reflects the ability of the grain boundary to resist deformation. Table 2 lists characteristic values of SW WNiFe and SW WNiFe-0.5ZrC alloys. The P value of SW WNiFe-0.5ZrC is about 0.211, which is higher than that of SW WNiFe (0.159). This could explain the higher strength of SW WNiFe-0.5ZrC.

The relationship between elongation and microstructure in WHAs can be expressed by the following empirical formula[29–30]:

$$\varepsilon = \varepsilon_0 + kV_{\mathrm{m}}(1 - C_{\mathrm{WW}}) \tag{4}$$

where ε is the elongation of WHAs, ε_0 and k are nonnegative constants. For ease of description, the value of $V_{\mathrm{m}}(1-C_{\mathrm{WW}})$ is abbreviated as Q. It can be seen that the elongation of WHAs at RT is closely related to the microstructural parameters V_{m} and C_{WW}. The Q value of SW WNiFe is 0.174, which is higher than that of SW WNiFe-0.5ZrC (0.159), as shown in Table 2. These results explain that the mechanical properties, especially ductility at RT of SW WNiFe alloy, are improved by LPS and hot rotary swaging.

To further elucidate the reasons for different performance of two alloys at different temperatures, the fracture morphologies of SW WNiFe and SW WNiFe-0.5ZrC alloys after tensile test were characterized, as shown in Fig. 10. Different types of fracture modes were found in these samples. Fig. 11 presents the schematic diagrams of four fracture modes of WHAs, including W cleavage, matrix (M) rupture, intergranular (W-W) fracture and W-matrix (W-M) failure. The fracture surface of SW WNiFe at RT (Fig. 10a) exhibits a relatively

Table 2 Characteristic values of SW WNiFe and SW WNiFe-0.5ZrC alloys

Material	C_{WW}	V_{m}/ vol%	P, $\left[\frac{C_{\mathrm{WW}}\left(1 - V_{\mathrm{m}}\right)}{dV_{\mathrm{m}}}\right]^{\frac{1}{2}}$	Q, $V_{\mathrm{m}}(1-C_{\mathrm{WW}})$
SW WNiFe	0.33±0.04	26	0.159±0.010	0.174±0.011
SW WNiFe-0.5ZrC	0.31±0.03	23	0.211±0.010	0.159±0.007

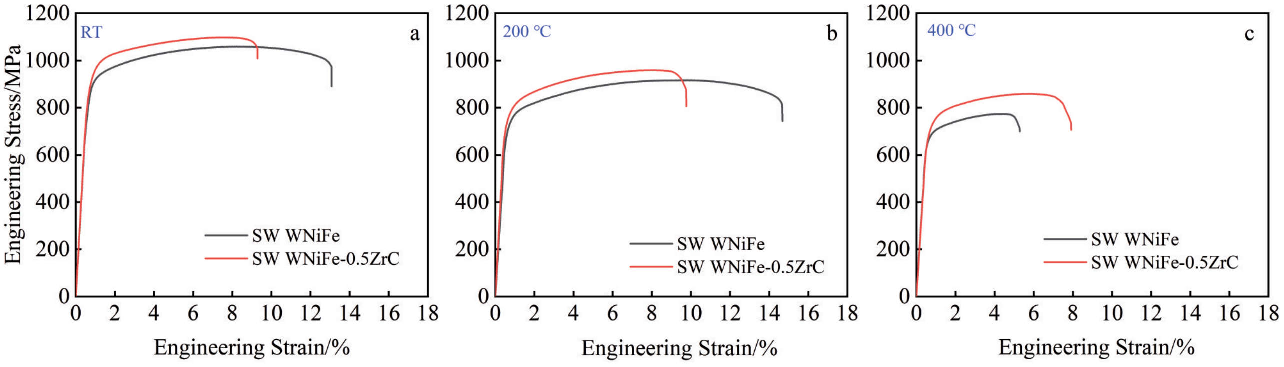

Fig.9 Engineering stress-engineering strain curves of SW WNiFe and SW WNiFe-0.5ZrC tested at RT (a), 200 °C (b), and 400 °C (c)

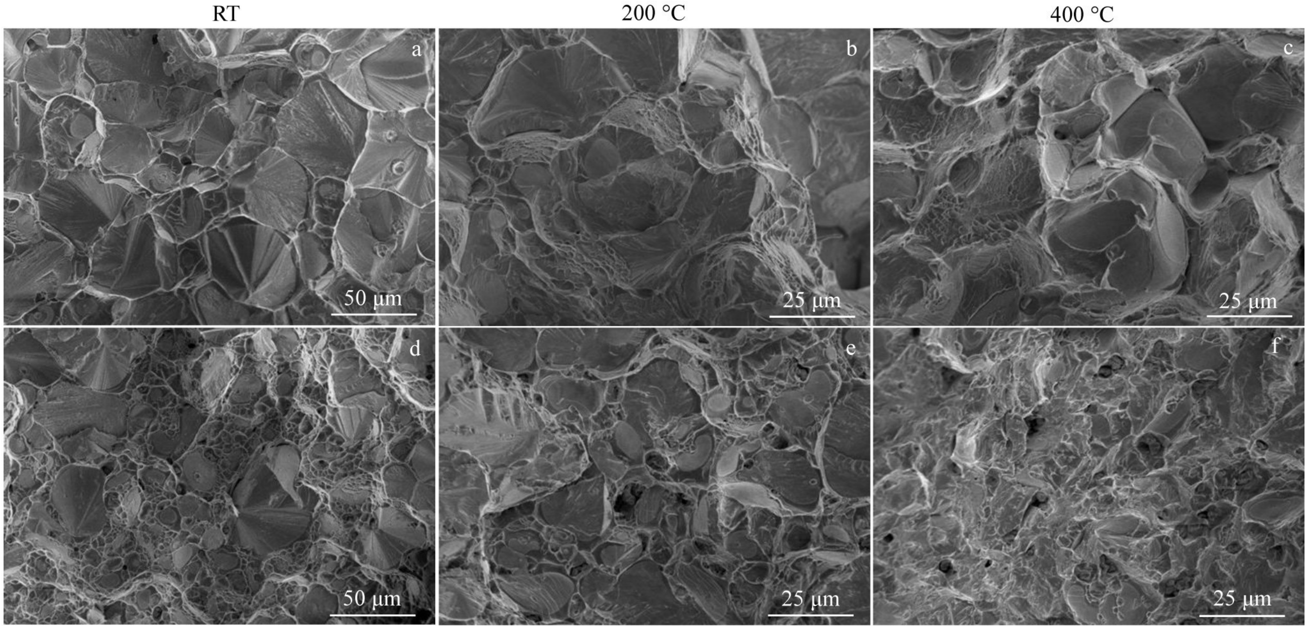

Fig.10 SEM images of fracture surfaces of SW WNiFe (a–c) and SW WNiFe-0.5ZrC (d–f) alloys after tensile test at different temperatures: (a, d) RT; (b, e) 200 °C; (c, f) 400 °C

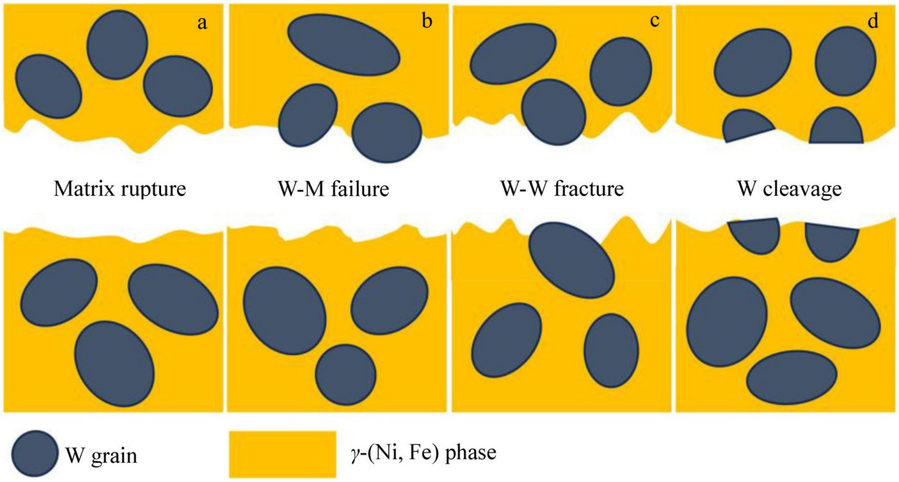

Fig.11 Schematic diagrams of fracture modes in WHAs: (a) matrix rupture, (b) W-M failure, (c) W-W fracture, and (d) W cleavage

smooth and flat surface with the matrix phase uniformly encapsulated around the W grains, and its fracture type is mainly composed of three kinds of fracture patterns, namely W cleavage, matrix rupture and W-W intergranular fracture. In Fig. 10c, at 400 °C, the composition of the fracture mode changes significantly, the adhesion between the relatively low-melting-point matrix phase and the W grains gradually decreases, and the interface appears to be significantly deboned. Fig.10d shows that the addition of ZrC significantly changes the fracture morphology of the SW WNiFe alloy, with the matrix phase adhering around the W grains like a spider web. When the temperature increases to 200 and 400 °C, the fracture morphologies of SW WNiFe-0.5ZrC display little changes, as shown in Fig.10e–10f.

Fig. 12 shows the proportion distribution of fracture modes of SW WNiFe and SW WNiFe-0.5ZrC at RT and 400 °C. With the temperature increases from RT to 400 °C, the proportion of W cleavage in SW WNiFe significantly decreases, while the proportion of intergranular fracture significantly increases. The fracture mode of SW WNiFe at 400 °C is intergranular fracture dominated by the tearing of the matrix phase. Compared to SW WNiFe, SW WNiFe-0.5ZrC exhibits a lower percentage of W cleavage and a higher percentage of intergranular fracture and matrix rupture at RT. When the temperature rises to 400 °C, only a minor increase occurs in the proportion of matrix rupture, which implies the high ductility of SW WNiFe-0.5ZrC.

The influence factors of the fracture strength σ_b of WHAs can be correlated with the fracture mode using the following empirical formula[31]:

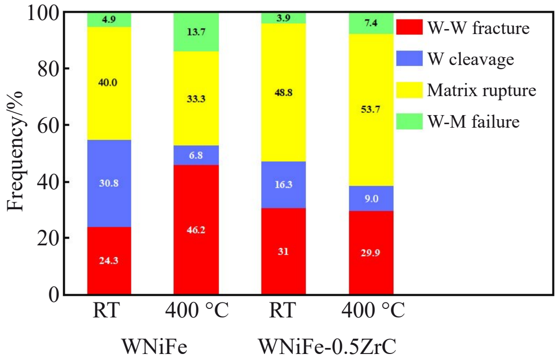

Fig.12 Schematic diagram of proportion of fracture modes at different temperatures

$$\sigma_b = f_W\sigma_W + f_{W-M}\sigma_{W-M} + f_M\sigma_M + f_{W-W}\sigma_{W-W} \quad (5)$$

where σ_W is the strength contribution of W cleavage, σ_{W-M} represents the strength contribution of W-M failure, σ_M represents the strength contribution of matrix rupture, and σ_{W-W} represents the strength contribution of W-W fracture. f_W, f_{W-M}, f_M and f_{W-W} represent the proportion fraction of corresponding fracture modes. The fracture strength of WHAs mainly comes from the first three items on the right side of Eq.(5).

It was suggested that the fracture behavior of WHAs at low temperatures (25–300 °C) is controlled by dislocation motion under Peierls stress, which mainly originates from bcc W grains occupying the vast majority of the volume fraction in WHAs, and the mechanical properties and fracture behavior are closely related to the W-M interfacial strength[32–33]. At RT, σ_{W-M} is significantly higher than σ_W and σ_M, and cracks are initiated from the interior of the W grains during tensile process, leading to transgrannular fracture as the dominant mode. It is worth noting that σ_{W-M} decreases obviously with increasing the temperature[34]. As the temperature increases from RT to 200 °C, the strength and fracture behavior of WHAs do not change significantly when σ_{W-M} remains higher than σ_W as a whole. At 400 °C and above, the deformation mechanism of WHAs has changed from the Peierls mechanism at RT to fcc metal-dominated forest intersection mechanism[33]. σ_{W-M} decreases significantly at 400 °C and the testing temperature is around DBTT of W. These lead to the decrease in strength and the change of fracture mode of SW WNiFe alloys at 400 °C. The above analysis results show that the softening and interfacial detachment of γ-(Ni, Fe) phase at high temperatures significantly reduce the strength and ductility of WHAs. While for the SW WNiFe-0.5ZrC alloy, the dispersed nanoscale particle can effectively improve the thermal stability and high temperature strength.

3.4 Thermal conductivity of SW WNiFe and SW WNiFe-0.5ZrC alloys

Fig. 13 shows the thermal conductivity of SW WNiFe, SW WNiFe-0.5ZrC and ITER grade pure W[35] from RT to 800 °C for comparison. The thermal conductivity of SW WNiFe and SW WNiFe-0.5ZrC alloys at RT is 72 and 70 $W\cdot m^{-1}\cdot K^{-1}$, respectively. The thermal conductivity of SW WNiFe is much lower than that of ITER grade pure W (173 $W\cdot m^{-1}\cdot K^{-1}$) at RT. However, with the increase in temperature, the thermal conductivity of pure W significantly decreases, drops to 140 $W\cdot m^{-1}\cdot K^{-1}$ at 400 °C, and further decreases to 121 $W\cdot m^{-1}\cdot K^{-1}$ at 800 °C. On the contrary, the thermal conductivity of SW WNiFe and SW WNiFe-0.5ZrC alloys shows upward trend at high temperatures, reaching about 100 $W\cdot m^{-1}\cdot K^{-1}$ at 800 °C, which is close to that of pure W. This result is consistent with the research results of Neu et al[7]. Considering that the working temperature of PFMs is usually above 800 °C, it can be inferred that the difference in thermal conductivity would be even smaller at higher temperatures, indicating that it is possible for WHAs to be used as PFMs of fusion reactors.

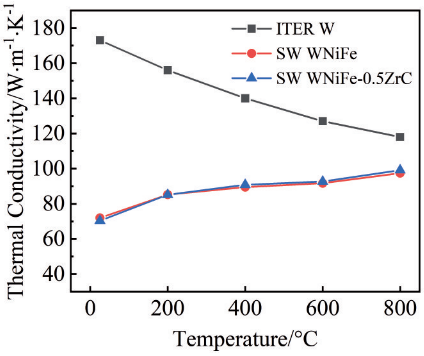

Fig.13 Thermal conductivity of SW WNiFe, SW WNiFe-0.5ZrC, and ITER grade pure W at different temperatures

4 Conclusions

1) The addition of ZrC nanoparticle can effectively refine the grains and improve the microhardness of WNiFe alloys. Nevertheless, the presence of ZrC nanoparticles hinders the formation of the γ-(Ni, Fe) phase during SPS. These could explain why SPS WNiFe-ZrC samples exhibit fine grains but are brittle at RT.

2) Through LPS and hot rotary swaging, the WNiFe and WNiFe-0.5ZrC alloys are ductile at RT and their tensile strength is significantly improved. The SW WNiFe-0.5ZrC has a high tensile strength of 1095 MPa and a TE of 9.3%, while most commercial pure bulk W is brittle at RT. The addition of ZrC nanoparticles inhibits the softening and interfacial detachment of γ-(Ni, Fe) phase at elevated temperatures, leading to improved high temperature strength and thermal stability. Compared with SW WNiFe, the SW WNiFe-0.5ZrC alloy shows finer grains, and it has both higher strength and better ductility at 400 °C. Besides, although WNiFe alloys exhibit low thermal conductivity at RT, their thermal conductivity is close to pure W at high temperatures.

3) WNiFe-ZrC alloys with room-temperature ductility, low cost and acceptable thermal conductivity at elevated temperatures may be used as potential candidates for PFMs in nuclear fusion reactors.

References

1 Zhao B L, Xia Y P, Zhang L F *et al. Materials Science and Engineering A*[J], 2022, 830: 142310

2 Wu Xuebang, Li Xiangyan, Zhang Yange *et al. Journal of Fusion Energy*[J], 2020, 39: 342

3 Linke J, Du J, Loewenhoff T *et al. Matter Radiation Extremes*[J], 2019, 4: 056201

4 Dubinko A, Yin C, Terentyev D *et al. International Journal of Refractory Metals and Hard Materials*[J], 2021, 95: 105409

5 Wang Chenrui, Dong Di, Ying Wenqing *et al. Rare Metal Materials and Engineering*[J], 2023, 52(10): 3600 (in Chinese)

6 Xie X F, Xie Z M, Liu R *et al. Acta Materialia*[J], 2022, 228: 117765

7 Neu R, Maier H, Balden M *et al. Fusion Engineering and Design*[J], 2017, 124: 450

8 Neu R, Maier H, Balden M *et al. Journal of Nuclear Materials*[J], 2018, 511: 567

9 Wang Zitong, Dong Di, Xiong Ning *et al. Rare Metal Materials and Engineering*[J], 2024, 53(5): 1229

10 Zhu Wentan, Liu Wensheng, Ma Yunzhu *et al. Journal of Materials Research and Technology*[J], 2021, 11: 2037

11 Feng Guorui, Yang Xinyu, Bai Jinwen *et al. Theoretical and Applied Fracture Mechanics*[J], 2023, 125: 103849

12 Alam M E, Wang Jing, Henager C H *et al. Materials Science and Engineering A*[J], 2021, 824: 141738

13 Alam M E, Odette G R. *Acta Materialia*[J], 2020, 186: 324

14 Yao Gang, Liu Xuepeng, Zhao Zhihao *et al. Materials & Design*[J], 2021, 212: 110249

15 Lv Yongqi, Han Yong, Zhao Siqi *et al. Journal of Alloy and Compounds*[J], 2021, 855: 157366

16 Chen Zheng, Yang Junjun, Zhang Lin *et al. Materials Characterization*[J], 2021, 175: 111092

17 Wang Hui, Ding Chenshi, Xie Zhuoming *et al. Rare Metal Materials and Engineering*[J], 2024, 53(5): 1321 (in Chinese)

18 Xie X F, Jing K, Xie Z M *et al. Materials Science and Engineering A*[J], 2021, 819: 141496

19 Jing K, Liu R, Xie Z M *et al. Acta Materialia*[J], 2022, 227: 117725

20 Xie Z M, Liu R, Miao S *et al. Scientific Reports*[J], 2015, 5: 16014

21 Yin Chao, Terentyev D, Zhang Tao *et al. Journal of Nuclear Materials*[J], 2020, 537: 152226

22 Renterghem W V, Terentyev D, Balaji S *et al. Journal of Nuclear Materials*[J], 2021, 544, 152710

23 Li Zhibo, Zhang He, Zhang Guohua *et al. Composites Part B*[J], 2022, 236: 109817

24 Sun Xuwen, He Zhi, Yan Shuxin *et al. Powder Metallurgy Technology*[J], 2025, 43(1): 86 (in Chinese)

25 Fan Jinglian, Gong Xing, Huang Baiyun *et al. Journal of Alloys and Compounds*[J], 2010, 489: 188

26 Ryu H J, Hong S H, Lee S *et al. Metals and Materials International*[J], 1999, 5: 185

27 Lee K H, Cha S I, Ryu H J *et al. Materials Science and Engineering A*[J], 2007, 458: 323

28 Armstrong A N. *Pharmaceutical Experimental Design and Interpretation*[M]. London: CRC Press, 2006: 45

29 Hu Ke, Li Xiaoqiang, Ai Xuan *et al. Materials Science and Engineering A*[J], 2015, 636: 452

30 Churn K S, German R M. *Metallurgical and Materials Transactions A*[J], 1984, 15: 331

31 Kiran U R, Venkat S, Rishikesh B *et al. Materials Science and Engineering A*[J], 2013, 582: 389

32 Christian J W. *Metallurgical and Materials Transactions A*[J], 1983, 14: 1237

33 Das J, Sarkar R, Rao G A *et al. Materials Science and Engineering A*[J], 2012, 553: 119

34 Gong Xing, Fan Jinglian, Ding Fei. *Materials Science and Engineering A*[J], 2015, 646: 315

35 Barabash V. *Summary of Materials Properties for Structural Analysis of the ITER Internal Components*[R]. Saint-Paul-lès-Durance: ITER Organization, 2015

纳米ZrC增强WNiFe合金的微观结构及性能

杨润[1,2]，王慧[2]，刘瑞[1,2]，吴学邦[2]，王先平[2]，方前锋[1,2]，刘长松[2]

(1. 中国科学技术大学，安徽 合肥 230026)

(2. 中国科学院 合肥物质科学研究院 固体物理研究所，安徽 合肥 230031)

摘　要：分别通过放电等离子烧结和旋锻制备了纳米ZrC颗粒强化的93W-4.9Ni-2.1Fe合金。结果表明，少量纳米ZrC颗粒的添加可以细化晶粒并提高WNiFe合金的硬度，但会阻碍烧结过程中γ-(Ni,Fe)相的形成。因此，放电等离子体烧结的WNiFe和WNiFe-ZrC合金在室温下是脆性的。而采用无压液相烧结和旋锻制备的WNiFe及WNiFe-0.5ZrC（wt%）合金具有室温塑性。在400 ℃时，旋锻WNiFe-0.5ZrC的抗拉伸强度和延伸率均高于WNiFe合金。纳米颗粒在W晶粒和γ-(Ni,Fe)相中分布，能够钉扎位错和晶界，显著提高合金强度。旋锻WNiFe-0.5ZrC的室温热导率仅为71 $W\cdot m^{-1}\cdot K^{-1}$，但在800 ℃时增加到约100 $W\cdot m^{-1}\cdot K^{-1}$，与纯W的热导率（121 $W\cdot m^{-1}\cdot K^{-1}$）相近，具有用于聚变堆的面向等离子体材料的潜力。

关键词：钨合金；ZrC；弥散强化；微观结构；导热性能

作者简介：杨润，男，1998年生，博士生，中国科学技术大学，安徽 合肥 230031，电话：0551-65591727，E-mail：yangrun@mail.ustc.edu.cn